Profiling the off-center atomic displacements in CuCl at finite temperatures with a deep-learning potential

Zhi-Hao Wang [ORCID],[1] Xuan-Yan Chen [ORCID],[1] Zhen Zhang [ORCID],[2] Xie Zhang [ORCID],[1,*] and Su-Huai Wei [ORCID][1,†]

[1]*Materials and Energy Division, Beijing Computational Science Research Center, Beijing 100193, China*
[2]*State Key Laboratory for Mechanical Behavior of Materials, Xi'an Jiaotong University, Xi'an 710049, China*

Cuprous halides (CuX, X = Cl, Br, or I) have been extensively investigated in the literature, but there still exist debates on whether the ground-state structures of CuX are zinc blende. By performing molecular dynamics simulations at finite temperatures with a newly developed accurate deep-learning potential for CuCl, we find that, in the absence of accurate exchange interactions, there exist collective off-center displacements of Cu, leading to the formation of large complex Cu cluster structures. However, these cluster structures are unstable once exchange interactions are properly included. Nevertheless, due to strong anharmonicity, thermal fluctuations could also lead to sizable off-center Cu displacements, resulting in instantaneous small Cu clusters. Still, these cluster configurations are not stable or metastable in the ground state. We thus unambiguously demonstrate that, although anharmonic off-center displacements of Cu are present in CuCl at finite temperatures, zinc blende is still the thermodynamically most favorable phase. These insights are critical to the understanding of liquidlike anharmonic behavior of Cu atoms in various Cu-containing compounds, which impacts a number of important properties such as thermal conductivity, ferroelectricity, and superconductivity.

I. INTRODUCTION

Cuprous halides (CuX, X = Cl, Br, or I) are wide-band-gap semiconductors with promising applications in electronic and optoelectronic devices [1–4]. In particular, being a native p-type semiconductor, the transparent CuI film has not only been employed as a hole transport material in solar cells [5–7], but also has shown exceptional performance as a thermoelectric material [8–10]. However, despite their wide applications, a thorough microscopic understanding of why this class of ionic crystals maintains a zinc-blende structure is still lacking. Highly ionic materials usually prefer the rocksalt structure. There is actually a critical threshold for the ionicity [11], above which the rocksalt structure with six-fold coordination is preferred and below which four-fold-coordination structures such as diamond, zinc blende, or wurtzite are favored. The ionicities of cuprous halides are near the critical threshold, leading to many anomalies.

Among the cuprous halides, CuCl is the most puzzling. Most notably, it has been speculated that CuCl is structurally disordered at room temperature with the Cu ions showing large displacements away from their tetrahedral sites in the zinc-blende crystal structure. Wei *et al.* [12] reported the existence of metastable secondary energy minima with low energy barriers when Cu moves along the four [111] antibonding directions [Fig. 1(a)] by performing first-principles calculations within the local density approximation (LDA). The presence of the metastable energy minima was rationalized in terms

of s-d coupling. More specifically, due to the small energy difference between occupied Cu $3d$ orbitals and unoccupied $4s$ orbitals, these states could interact strongly. However, in an ideal zinc-blende structure the coupling between Cu $3d$ and $4s$ states is symmetry forbidden. But, once Cu displaces away from the center of the tetrahedron, the coupling between Cu $3d$ and $4s$ states becomes allowed, which significantly reduces the total energy and destabilizes the zinc-blende structure [Fig. 1(a)]. Later, it was further reported that collective off-center displacements of four neighboring Cu atoms in a larger supercell (32 atoms) may form a "Cu$_4$" local configuration [13] [Figs. 1(b)–1(d)], the energy of which is even lower than that of the ideal zinc-blende structure [see the curves for CuBr and CuCl in Fig. 1(b)]. Similarly, if the displacement is along the [100] direction, a more distorted "Cu$_7$" configuration can be formed in a 64-atom supercell of zinc-blende CuCl [14] [Fig. 1(e)]. In short, theoretical calculations suggested that the ground state of CuCl may not be zinc blende, which was, however, never observed in experiments [15–19].

To resolve this puzzle, we have recently systematically investigated the structural anomalies in zinc-blende cuprous halides in comparison with other typical semiconductors based on accurate first-principles calculations [20,21]. We showed that the discrepancy between theory and experiment in early studies stems from inaccurate treatments of the exchange interactions in the local (LDA) or semilocal Perdew-Burke-Ernzerhof (PBE) [22] functionals. With an accurate Heyd-Scuseria-Ernzerhof (HSE) [23] hybrid functional, the Cu$_4$ configuration was found to be unstable in all cuprous halides [20,21], agreeing well with experiments. For CuCl, as the exchange contribution increases, the empty s states get pushed up in energy and the occupied d states significantly

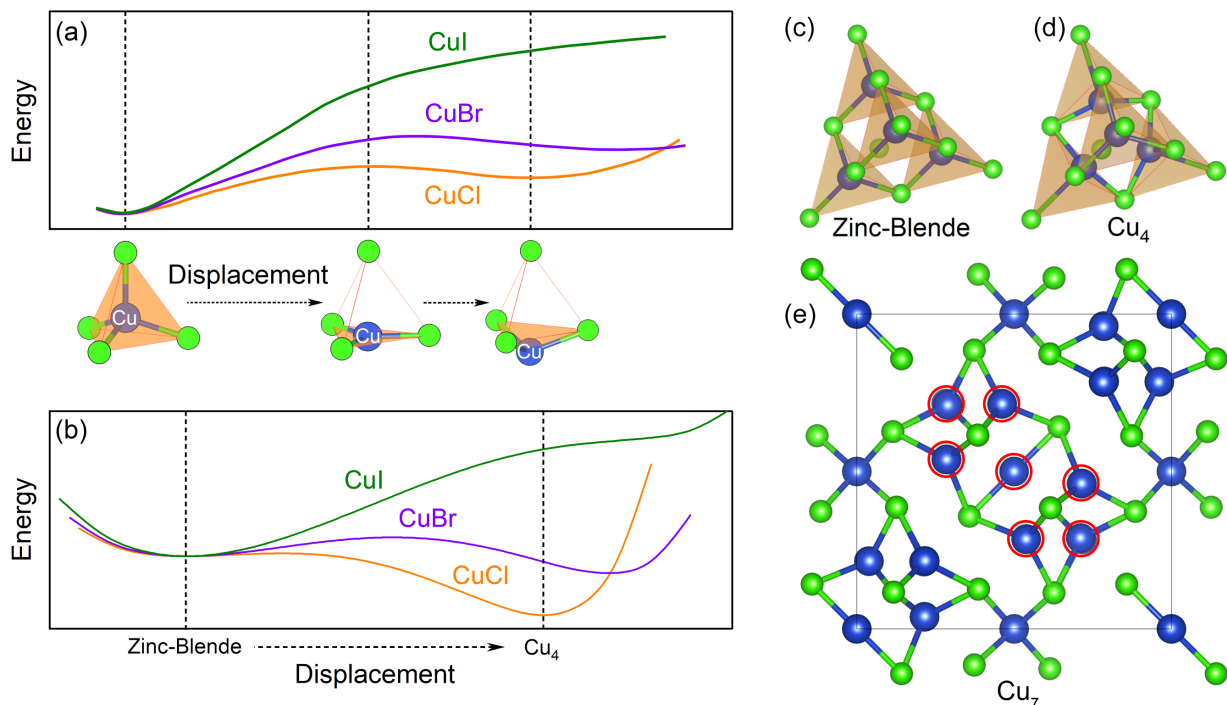*xiezhang@csrc.ac.cn
†suhuaiwei@csrc.ac.cn

FIG. 1. Potential energy as a function of the displacement of (a) one Cu atom and (b) four Cu atoms (Cu$_4$) from the center of the halide tetrahedron toward the face center of the tetrahedron in CuX. Perspective views of (c) zinc-blende structure and (d) Cu$_4$ configuration. (e) Front view (along the [100] direction) of the distorted Cu$_7$ configuration (seven Cu atoms in red circles). The central Cu atom is displaced along the [100] direction.

drop in energy; the enhanced *s-d* energy separation weakens *s-d* coupling and decreases its impact on the total energy. Consequently, the Cu atoms would prefer to stay at the centers of the tetrahedra. The same physics holds for CuBr and CuI as well. Hence we concluded that exchange interactions play a decisive role in stabilizing zinc-blende cuprous halides.

However, systematic studies of different possible cluster configurations and their stabilities at finite temperatures are still missing. In particular, there might be cluster configurations beyond the already known Cu$_4$ and Cu$_7$ structures; it is also unclear if those configurations are also unstable once the exchange interactions are properly included and how they behave at finite temperatures. To answer these questions, a typical strategy would be performing *ab initio* molecular dynamics (AIMD) simulations with accurate hybrid functionals. While AIMD has become computationally affordable for reasonably sized supercells with, typically, a few hundred atoms, practical cases are mostly carried out with local or semilocal exchange-correlation functionals. Conducting AIMD simulations with accurate hybrid functionals is still computationally prohibitive for large supercells, which means that these calculations would only be possible with relatively small supercells, making the examination of large complex Cu cluster configurations extremely challenging. Thus it is critical to find a computationally more effective way to take into account the exchange interactions, enabling AIMD simulations for large-scale systems. A plausible solution is to develop accurate and transferrable interatomic potentials for these materials based on machine learning, such as deep-learning potentials for molecular dynamics (DeePMD) [24,25].

In this work, to solve the dilemma of accuracy versus efficiency, we develop an interatomic potential based on the DeePMD formalism for the zinc-blende CuCl system, which enables us to carry out large-scale molecular dynamics (MD) simulations at finite temperatures. The models are trained by fitting to accurate first-principles data generated employing the HSE hybrid functional for affordable small supercells, which enables systematic profiling of the anharmonic off-center atomic displacements in CuCl at finite temperatures. A similar potential is trained with data sets generated using the PBE functional, which is employed for a comparative study. With the newly developed deep-learning potentials for CuCl, we find that there indeed exist complex large Cu cluster configurations (beyond Cu$_4$ and Cu$_7$) when exchange interactions are not included (i.e., using the PBE-based potential). However, these clusters are unstable once exchange interactions are properly taken into account (i.e., using the HSE-based potential). Still, thermal fluctuations could lead to pronounced off-center Cu displacements due to strong anharmonicity, leading to instantaneous small Cu clusters. Nevertheless, these cluster configurations are not stable or metastable in the ground state. In above, we conclude that zinc-blende CuCl is indeed thermodynamically stable against off-center displacements of Cu atoms, which should also apply to CuBr and CuI, since the lattice anharmonicity in these two materials is even weaker.

This paper is organized as follows. In Sec. II, we describe the details of data set preparation, training method, and performance of the deep-learning potentials. In Sec. III, we illustrate an application of the trained deep-learning potential
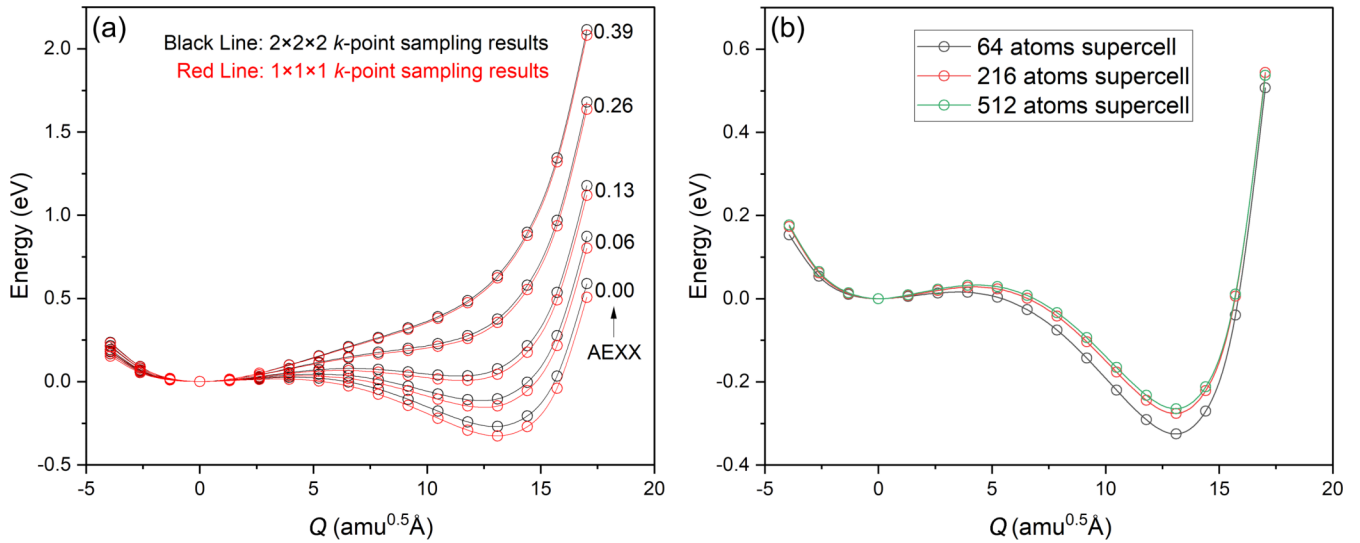
FIG. 2. Total energy (referenced to the energy of zinc-blende structure) as a function of configuration coordinate Q (in units of amu$^{0.5}$ Å; see detailed definition for Q in, e.g., Ref. [28]) in CuCl while varying the fraction of the nonlocal Fock exchange (the AEXX parameter) in the HSE hybrid functional. An AEXX of 0.39 corresponds to the case where the theoretically computed band gap agrees with the experimental value. (a) Benchmark tests regarding Γ-point mesh (red lines) and $2 \times 2 \times 2$ k-point mesh (black lines) with different exchange mixing parameter (zero represents PBE). (b) Benchmark tests regarding different sizes of CuCl supercells (64, 216, and 512 atoms) using the PBE functional with Γ-point sampling.

to studying the sophisticated atomic structure of CuCl at finite temperatures. Section IV summarizes and concludes this work.

II. DEVELOPMENT OF DEEP-LEARNING POTENTIAL

A. Preparation of training data sets

In this study, we employ a practically affordable supercell (64 atoms, comprising 32 Cu and 32 Cl) for AIMD simulations with the HSE hybrid functional using the Vienna *ab initio* simulation package (VASP) [26,27]. To be more specific, the HSE hybrid functional used here adopts a screening parameter μ of 0.2 Å^{-1}. The Brillouin zone is sampled using the Γ point. The energy cutoff of the plane-wave basis is set to 500 eV. By performing benchmark tests regarding k-point mesh [Fig. 2(a)] and supercell size [Fig. 2(b)], we find that it is sufficiently accurate to use a 64-atom supercell with Γ-point sampling to perform our calculations in order to capture the key physics of concern. We note that, although here we mainly focus on the difference between the PBE and HSE functionals, the key is to correctly describe the s-d coupling, which can be well reproduced by using the PBE+U approach with a properly benchmarked U parameter on the Cu $3d$ orbitals.

The procedure of preparing data sets is as follows. First, the primitive cell of zinc-blende CuCl is relaxed using the HSE hybrid functional to obtain the optimal lattice constant. The atomic positions and cell shape and volume are all fully relaxed during the energy and force minimizations. The convergence criteria employed for structural relaxations are set to 10^{-5} eV for energy and 0.01 eV Å^{-1} for force. Next, the relaxed two-atom primitive cell is expanded into a cubic 64-atom supercell. This supercell is employed as the initial configuration for the AIMD simulations. Finally, AIMD

simulations are carried out at 300 K for 10 ps (10 000 time steps) in the canonical (*NVT*) ensemble, during which the total energies of the system and the forces of individual atoms are calculated at every time step.

The AIMD simulations are performed using the HSE functional with the nonlocal-Fock-exchange mixing parameter set to 0.39 in order to reproduce the experimental band gap of CuCl, i.e., 3.399 eV [20,29,30]. In principle, the fraction of the nonlocal Fock exchange can also be determined by benchmarking against the experimental lattice constants. However, in the present case the lattice parameter only changes slightly when we use the PBE functional (5.426 Å) and the HSE functional with 0.39 mixing (5.454 Å). Hence we focus on reproducing the experimental band gap, which also yields a more accurate description of the s-d separation and coupling [21].

The 10 000 frames of data are used for deep-learning potential training in the subsequent section. The first 80% of the data set are used as the training set and the remaining data are employed for validation. In order to accurately capture the physical properties at a wider range of volume, we extend our training data set by including another three AIMD simulations with the functional and temperature identical to the previous simulation: one in the *NPT* ensemble and another two in the *NVT* ensemble with smaller and larger volumes than the initial supercell, respectively. Each of the three simulations are performed for 1 ps (1000 time steps) to obtain 1000 frames of data for training.

To illustrate the importance of the exchange interactions, we also perform another set of AIMD simulations using the PBE functional, with other settings all identical to previous simulations using the HSE functional, with which we develop another deep-learning potential for CuCl with the PBE level of accuracy.

B. Training of the deep-learning potential

In this work, the trainings are performed using the deep-learning package for many-body potential energy representation and molecular dynamics (DeePMD-kit) [31] within the deep-learning potential generator (DP-GEN) [32]. Considering a system of N atoms in a three-dimensional Euclidean space, the local environment matrix R_i of the ith atom is defined as an $N_i \times 3$ matrix, which contains the relative coordinates of N_i atoms included in a sphere centered at the coordinate of the ith atom with a predefined cutoff radius r_c. By definition, the local environment matrix preserves the translational symmetry. Further, for each atom i, the symmetric matrix $\Omega^i = R^i(R^i)^T$ is an overcomplete array of invariants with respect to translation and rotation. However, this symmetric matrix switches rows and columns under a permutational operation. Thus a feature matrix D_i is defined to guarantee the translational, rotational, and permutational symmetries at the same time by taking an embedding procedure.

The potential energy E of the system is decomposed into atomic-energy contributions:

$$E = \sum_i E_i, \qquad (1)$$

where i denotes the indexes of the atoms. Each atomic energy E_i is determined by the local environment of the ith atom:

$$E_i = E_i(D_i\{R_i\}), \qquad (2)$$

where D_i is the feature matrix and R_i is the local environment matrix. The whole preprocessing is solved in three steps.

First, R_i is converted to the generalized local environment matrix $\widetilde{R}_i$ referring to the formula

$$R_i = \{x_{ji}, y_{ji}, z_{ji}\} \mapsto \widetilde{R}_i = \frac{S(r_{ji})}{r_{ji}}\{r_{ji}, x_{ji}, y_{ji}, z_{ji}\}, \qquad (3)$$

where $S(r_{ji})$ is a continuous and differentiable scalar weighting function applied to each component, defined as

$$S(r_{ji}) = \begin{cases} \frac{1}{r_{ji}}, & r_{ji} < r_{cs}, \\ \frac{1}{r_{ji}}\left[\frac{1}{2}\cos\left(\pi \frac{r_{ji}-r_{cs}}{r_c-r_{cs}}\right) + \frac{1}{2}\right], & r_{cs} < r_{ji} < r_c, \\ 0, & r_{ji} > r_c. \end{cases} \qquad (4)$$

Here r_{cs} is a smooth cutoff parameter, r_c is the cutoff radius, and $r_{ji} = |\mathbf{r}_{ji}| = |\mathbf{r}_j - \mathbf{r}_i| \leqslant r_c$.

Second, through an encoding network, $\widetilde{R}_i$ mapped to the embedding matrix G^{i1} and G^{i2}.

Third, the matrix D_i can be defined through the product of matrices:

$$D_i = (G^{i1})^T \widetilde{R}_i(\widetilde{R}_i)^T G^{i2}. \qquad (5)$$

Using D_i as the input node of the fitting neural network, E_i as output node is obtained after linear and nonlinear transformation. The total energy of the system can be obtained by adding resulting E_i. In addition, since the resulting function is smooth, the force can be expressed as $F_i = -\nabla_{r_i} E$. The embedding and fitting neural networks are optimized via minimization of loss functions:

$$L(p_f, p_\varepsilon) = \frac{p_f}{3N}\sum_i |\Delta F_i|^2 + p_\varepsilon \Delta\varepsilon^2, \qquad (6)$$
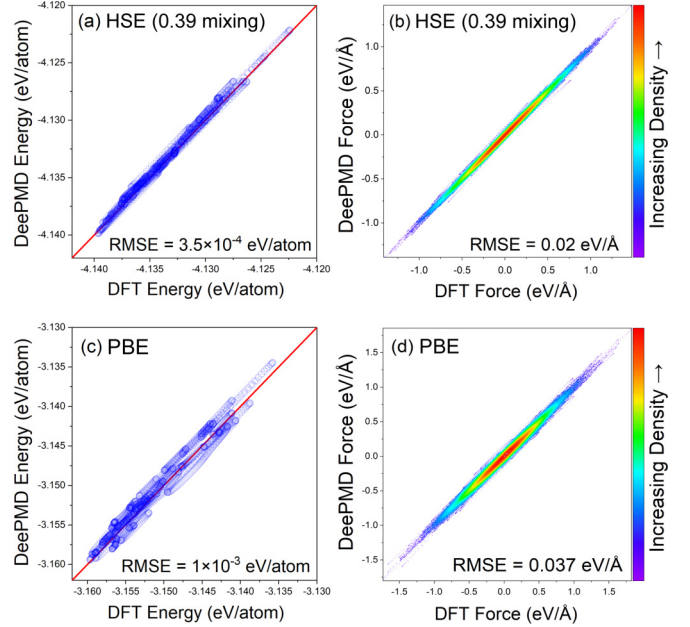

FIG. 3. Comparison of the energy and forces computed with the DeePMD kit with respect to the reference DFT data for the same configurations: (a),(c) energy per atom in the configuration: (a) HSE-based potential and (c) PBE-based potential; (b),(d) the corresponding atomic forces: (b) HSE-based potential and (d) PBE-based potential.

where ΔF_i and $\Delta\varepsilon$ are the force difference on the ith atom and the energy difference per atom, respectively. N is the total number of particles. p_ε and p_f are tunable prefactors. Readers are encouraged to revisit [31,33] for further details.

In this work, the smooth version of the deep-learning potential model is adopted [33]. The smooth cutoff parameter (r_{cs}) is chosen to be 0.5 Å. The radial cutoff (r_c) is taken as 6 Å. That means the inverse distance $1/r$ decays smoothly from 0.5 Å to 6 Å in order to remove the discontinuity introduced by the cutoff, which is sufficient to capture atoms in the first coordination shell. The embedding network of size [25, 50, 100] follows a residual-network-like architecture [34]. The fitting network is composed of three layers, with each containing 240 nodes. The Adam stochastic gradient descent method [35] is used and the learning rate decreases exponentially from 1.0×10^{-3} to 3.5×10^{-8}. The decay rate is approximately 0.95 and the decay step is set to 5000. The tunable prefactors in the loss functions ($p_\varepsilon^{\text{start}}$, p_f^{start}, $p_\varepsilon^{\text{limit}}$, and p_f^{limit}) are set to 0.02, 1000, 1, and 1, respectively.

C. Performance of the deep-learning potential

When the training completes, the potential is tested to verify its accuracy. Figure 3 illustrates the quality of the trained potentials for zinc-blende CuCl based on density-functional theory (DFT) calculations with the HSE and PBE functionals. In the case of a perfect matching, all data points plotted in Figs. 3(a)–3(d) would be strictly on the diagonal line. One can see that most points lie in a close vicinity of the diagonal. The root-mean-square errors (RMSEs) of energies and forces for validation shown at the corner in Figs. 3(a)–3(d)

TABLE I. Comparison of computed properties of zinc-blende CuCl, including lattice parameter a in Å, bulk modulus B in GPa, and elastic constants C_{ij} in GPa.

	Expt.	HSE		PBE	
		DFT	Potential	DFT	Potential
a (Å)	5.420[a]	5.464	5.471	5.436	5.456
B (GPa)	65[a],40[b]	48	47	49	52
C_{11} (GPa)	45[b]	55	55	56	59
C_{12} (GPa)	37[b]	45	43	45	49
C_{44} (GPa)	15[b]	16	15	15	15

[a]Reference [36].
[b]Reference [37].

are sufficiently small, validating the accuracy of the newly developed deep-learning potentials in predicting energies and atomic forces.

In addition to basic tests for energy and force, we also check the performance of the deep-learning potentials in describing the basic properties for the zinc-blende phase of CuCl (γ-CuCl) (see Table I). It is evident from the table that our deep-learning potentials can well reproduce the DFT data with either the HSE or PBE functionals and agree well with the experimental results.

In Fig. 4, we compare the energy-volume curves obtained from DFT and the two potentials. One can see that, within a wide range of volume, the predictions of the potentials agree well with the DFT results, which further demonstrates the accuracy of the newly developed potentials for a wide range of volume.

For our current investigation, a key quantity of interest is the potential energy surface with respect to the off-center displacements of Cu, for which we carefully benchmark in Fig. 5. Here we present the energy variation with respect to the collective off-center displacements of four neighboring Cu atoms (Cu_4), using a 64-atom supercell for CuCl. We introduce the Cu_4 configuration and then relax the structure. The HSE result shows that the zinc-blende structure is the most stable configuration, being consistent with the experimental observation. The PBE data give the opposite trend that the Cu_4 configuration seems to be more stable, due to the underestimated s-d separation resulting from the semilocal PBE functional. Our deep-learning potentials capture well the different trends that the HSE and PBE results exhibit, respectively (see Fig. 5).

To further assess the accuracy of the deep-learning potentials in computing finite-temperature properties, we compute the phonon spectra by means of the finite displacement method as implemented in the PHONOPY package [38]. Figure 6 shows the phonon band structures along high-symmetry directions in the Brillouin zone, which reveals remarkable agreement between the exact DFT results and the ones obtained from the deep-learning potentials. However, to demonstrate the importance of accurate exchange interactions for the vibrational properties, we also analyze the vibrational density of states (VDOS) of each phonon spectrum (see Fig. 7). Usually, within the Debye model of vibrational spectra, the VDOS at low energies is proportional to the
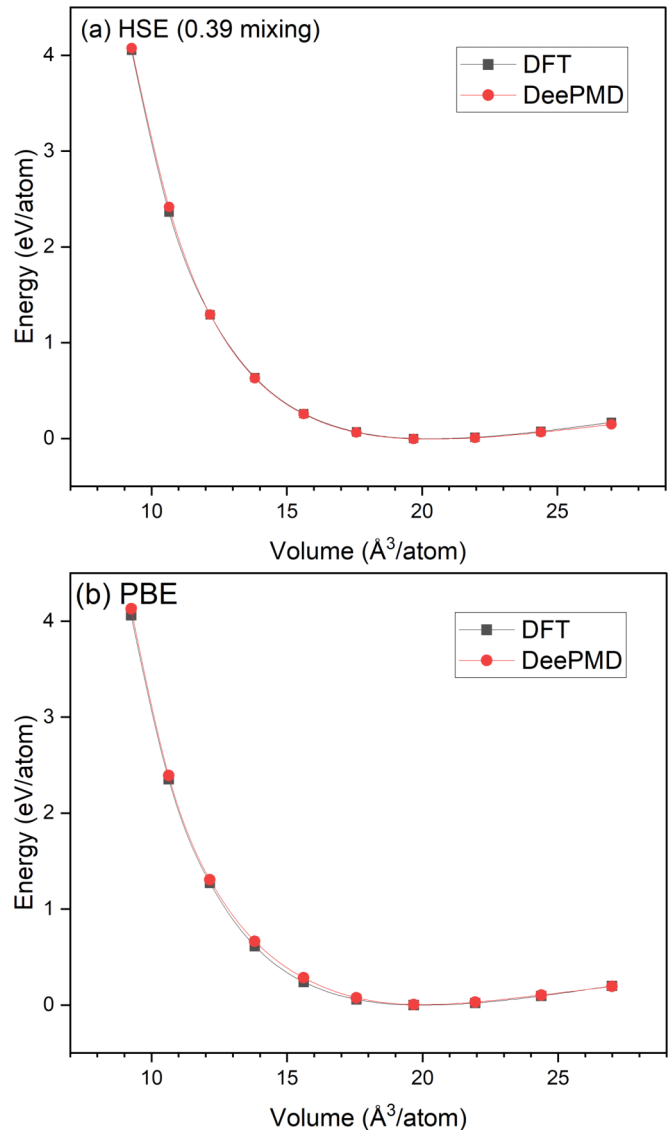

FIG. 4. Energy-volume curves described by DFT and deep-learning potentials (with the energy of the lowest configuration shifted to zero) derived from (a) HSE and (b) PBE data sets.

frequency squared. However, in some materials, their spectra depart from this law and result in peaks upon normalizing the VDOS by frequency squared, which are commonly referred to as the "boson peak" [39–41]. As depicted in Fig. 7(c), after normalizing the VDOS in Fig. 7(b) by the frequency squared, a significant peak appears in the PBE-based results, which is due to the fact that the PBE functional induces stronger anharmonicity than the HSE hybrid functional for CuCl, in agreement with our previous results (see Fig. 5). In particular, the boson peak derived from the PBE functional is much sharper than that from the HSE functional [Fig. 7(c)], which means that CuCl tends to be more disordered in the absence of accurate exchange interactions. More details will be discussed in the following section. Overall, based on these comparisons with DFT and the deep-learning potentials, we can conclude that both the HSE and PBE deep-learning potentials describe
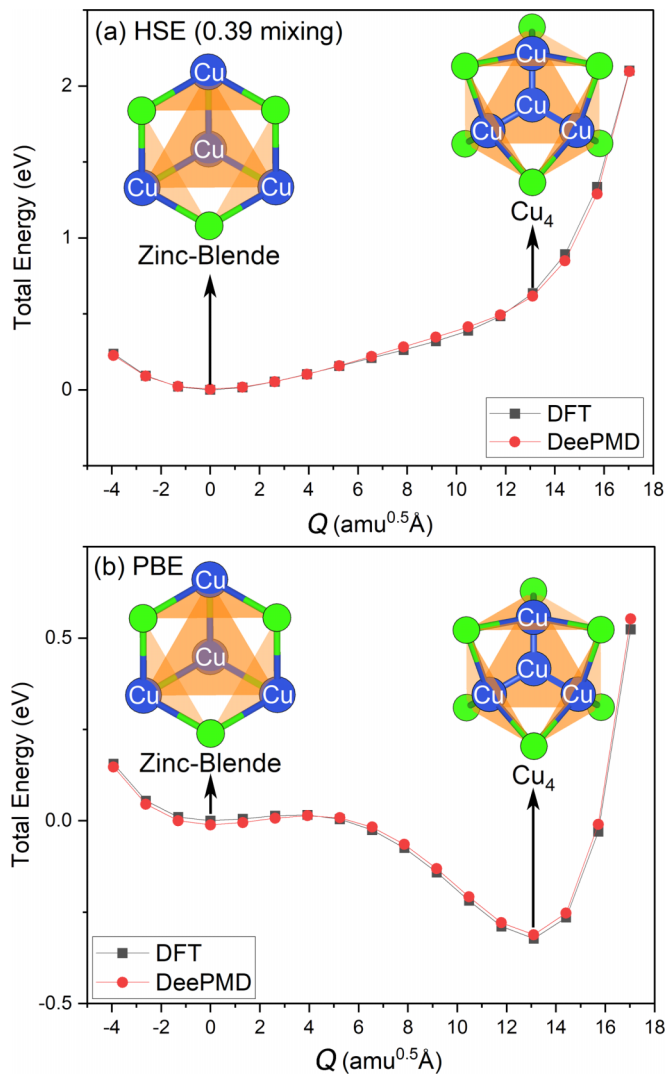
FIG. 5. Total energy (with the energy of zinc-blende structure shifted to zero) as a function of configuration coordinate Q (in units of amu$^{0.5}$ Å) in CuCl, described by DFT and deep-learning potentials derived from (a) HSE and (b) PBE data sets.

lattice vibrations very well, enabling a predictivity in finite-temperature properties.

III. ATOMISTIC SIMULATIONS WITH DEEP-LEARNING POTENTIALS

After checking the accuracy of the newly developed deep-learning potentials, we employ them to perform atomistic simulations of the finite-temperature properties of CuCl using the LAMMPS package [42]. The Nosé-Hoover thermostat [43,44], periodic boundary conditions, and the canonical ensemble are applied in the simulations. The initial simulation cell consists of 8000 atoms ($10 \times 10 \times 10$ supercells of the cubic unit cell). The simulations are run for 0.1 ns (100 000 time steps) for equilibration within the canonical ensemble. The damping parameters for the thermostat are chosen to be 0.01 ps. The MD simulations are performed at 100, 300, and 500 K, which are lower than the melting point of CuCl (696 K [45]).
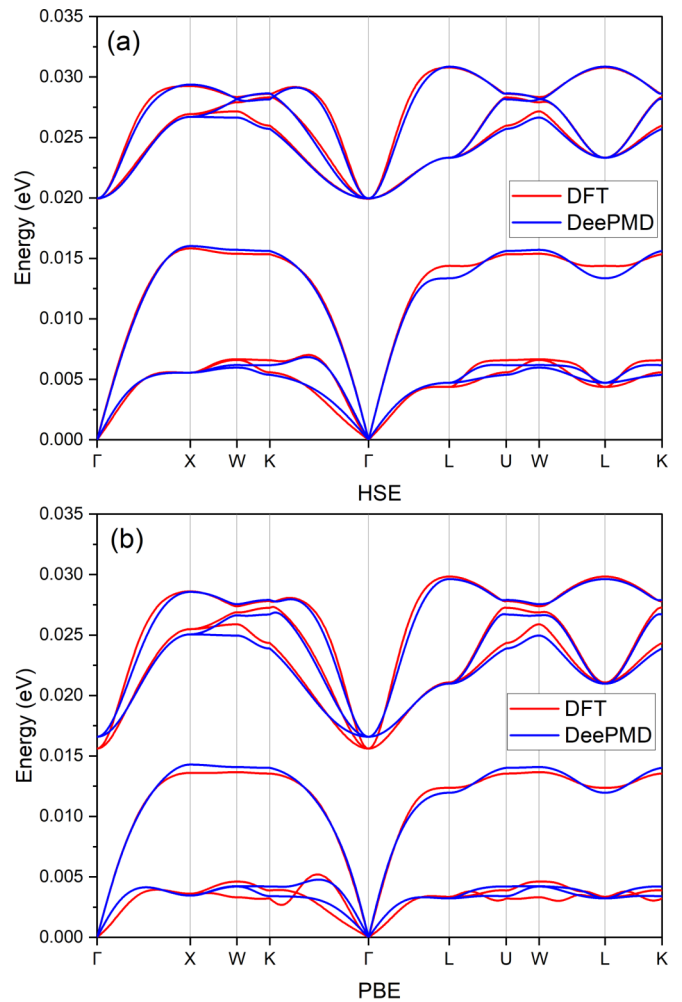

FIG. 6. Phonon dispersion spectra for zinc-blende CuCl described by DFT and deep-learning potentials derived from (a) HSE and (b) PBE data sets.

Before studying how temperature affects the off-center displacements of Cu atoms and thus the coordination number (CN) of Cu with Cl, we first analyze the partial radial distribution functions (PRDFs) of the Cu-Cl pair to determine a proper cutoff radius in the CN counting. In Fig. 8, one can see that, for the ideal zinc-blende structure, the bond length between Cu and neighboring Cl atoms is approximately 2.35 Å. For the deep-learning potential trained with the HSE data sets, as the temperature increases, the peaks at 2.35 Å in the PRDFs exhibit sizable broadening between 2.0 and 2.75 Å. Hence we choose 2.75 Å as the cutoff radius during the statistical evaluation of the CNs.

In Fig. 9, for the deep-learning potential trained with the HSE data sets, when the temperature is relatively low (100 K), almost all Cu atoms are in fourfold coordination, corresponding to the ideal zinc-blende crystal structure. As the temperature rises from 100 to 500 K, more and more Cu atoms move away from their tetrahedral sites. At room temperature (300 K), approximately 10% of Cu atoms are at off-center sites. This estimation is half of the one obtained by Park and Chadi, which was estimated based on the static strain energy computed from first principles using the LDA
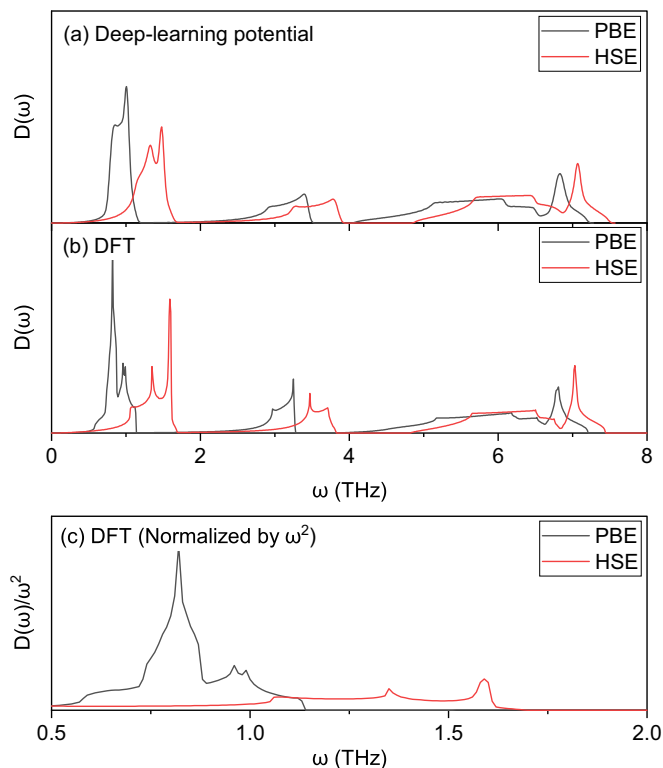
FIG. 7. Vibrational density of states (VDOS) $D(\omega)$ calculated using (a) the deep-learning potentials and (b) DFT with the PBE (black line) and HSE (red line) functionals. (c) VDOS normalized by the frequency squared, i.e., $D(\omega)/\omega^2$, for the same data in (b), but with a focus on the low-frequency region.

functional for a small supercell [13]. By contrast, the results given by the potential trained using PBE functional lead to an anomalous consequence: for all temperatures studied (100, 300, or 500 K), most of the Cu atoms (almost 60%) always prefer threefold coordination. Under this circumstance, the zinc-blende CuCl would be unstable at low temperatures.

To further investigate the Cu cluster configurations from MD simulations, we extract the properly equilibrated frames from the MD simulations performed at 300 K, analyze their PRDFs, and compare them with the PRDFs of the ideal zinc-blende structure. In Fig. 10, one can see that, for the deep-learning potential trained with the HSE data sets, the peaks in the PRDFs hardly move in position, but exhibit broadening due to the temperature-induced lattice vibrations compared to the ideal zinc-blende structure. By contrast, in the PRDFs of the potential trained using PBE functional, the first peak position of the Cu-Cu pair moves toward much lower distances. The qualitative differences in those PRDFs can be rationalized by the fact that the zinc-blende structure is stable within the HSE-based potential, but unstable within the PBE-based one. Hence the PBE-based simulations identify Cu atoms being energetically favorable at off-center sites, which leads to completely different PRDFs compared with the HSE case.

We further analyze the Cu clusters in the equilibrium configurations from MD simulations performed at 300 K using the deep-learning potential trained with PBE data sets [see
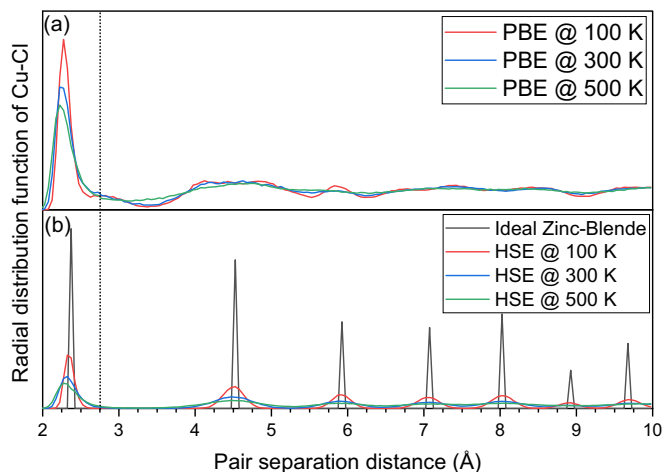

FIG. 8. Computed partial radial distribution functions (PRDFs) of the Cu-Cl pair in the ideal zinc-blende structure (black curve), the equilibrium configurations from the MD simulations performed using the deep-learning potentials trained with (a) PBE and (b) HSE data sets at 100 K (red curves), 300 K (blue curves), and 500 K (green curves). The vertical short dot line marks a specific value of 2.75 Å in the pair separation distance.

Fig. 11(a)]. In order to distinguish between different Cu clusters as much as possible, we choose a Cu-Cu distance cutoff of 3.2 Å, which sits in the middle between the average Cu-Cu distance in the ideal zinc-blende structure (approximately 3.8 Å) and the length of the Cu-Cu bonds if two Cu atoms displace along the [111] or equivalent antibonding directions to the face center of the tetrahedron (approximately 2.7 Å). In Fig. 11(a), one can see that most of the Cu clusters are
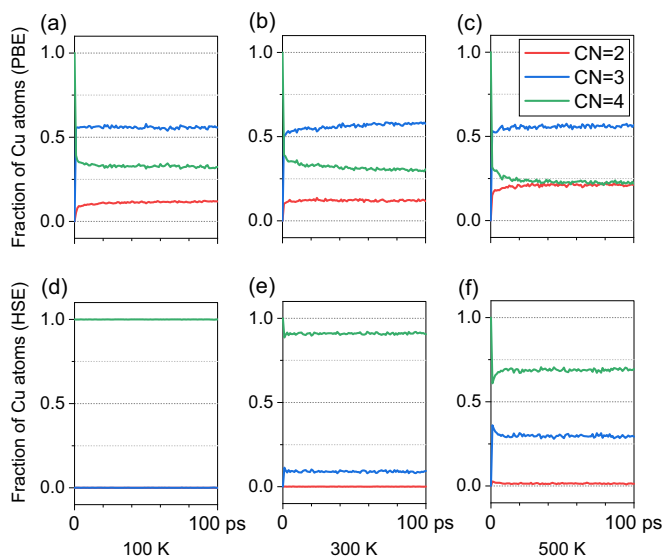

FIG. 9. Computed coordination number (CN) of Cu with neighboring Cl atoms as obtained from MD simulations performed at different temperatures using the deep-learning potentials trained with (a)–(c) PBE and (d)–(f) HSE data sets. For each subgraph, the horizonal axis stands for the number of MD steps and the vertical axis represents the ratio of Cu atoms with a specific CN to the total Cu atoms in the whole system.
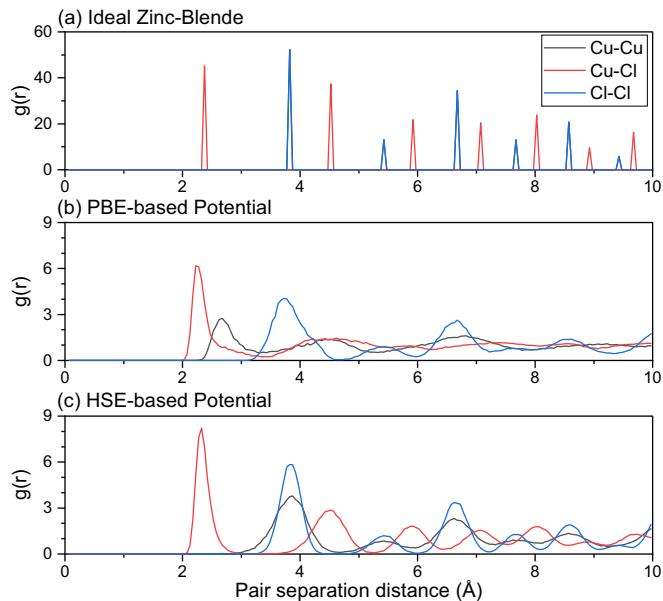
FIG. 10. Computed PRDFs of (a) the ideal zinc-blende structure, the equilibrium configurations from MD simulations performed at 300 K using the deep-learning potentials trained with (b) PBE and (c) HSE data sets. In zinc-blende structure, the PRDFs of Cu-Cu pair (black curve) and Cl-Cl pair (blue curve) completely overlap.

forming zigzag chain structures, which contain lots of Cu atoms. To examine whether these finite-temperature cluster configurations are stable or metastable ground-state structures, we perform structural relaxations for the structure at 0 K using the PBE-based potential [see Figs. 11(b) and 11(c)]. After relaxation, a new "defective" structure is gradually formed, which has lower total energy than zinc-blende, Cu_4, and even Cu_7 structures according to the PBE-based potential. The complete defective structure based on the PBE potential shows an amorphouslike phase, which explains the sharp boson peak revealed in Fig. 7(c). Since the sizes of the supercells in DFT calculations are limited, only small clusters like Cu_4 and Cu_7 rather than this large complex cluster configuration were observed in previous studies [13,14].

To further investigate the structural deviation of the new defective structure from the ideal zinc-blende structure, we cut a local volume out of the original large structure (see Fig. 12) and compare it with the ideal zinc-blende structure in three orthogonal directions ([001], [$\bar{1}10$], and [110]). As shown in Fig. 12, in a single chain of the new structure, two of the four neighboring Cu atoms are displaced to the face center of a tetrahedron along the [111] antibonding directions, transitioning from fourfold coordination to threefold coordination. The distance of these two Cu atoms changes from 3.8 Å (average Cu-Cu bond length in the ideal zinc-blende structure) to approximately 2.7 Å. This gives an explanation to the discrepancy in the PRDFs in Figs. 10(a) and 10(b) and reveals why most of the Cu atoms always prefer threefold coordination in Figs. 9(a)–9(c). Another two of the four neighboring Cu atoms move along the [001] direction, similar to the central Cu atom in the Cu_7 configuration mentioned above, shifting from fourfold coordination to twofold coordination. The displacement along the [001] direction is equivalent to a

superposition of displacements along two of the [111] directions, so the new defective structure is basically constructed by off-center displacements of Cu atoms along different [111] directions.

Figure 13 provides another comparison between the new defective structure and the Cu_7 configuration. As the figure shows, the new structure is mainly composed of two kinds of domains, which contain two groups of chains that are orthogonal to each other. In one of the domains, the structure far away from the domain wall is similar to the centering configuration of the Cu_7 cell [Figs. 13(a) and 13(d)]. Due to the periodic boundary condition, four corners of the Cu_7 cell can be combined into another substructure, which is identical but orthogonal to the centering configuration. The interface of the centering configuration and the substructure at the corner of the Cu_7 cell share many similarities with the structure of the domain wall in the new defective structure [Figs. 13(a)–13(c) and 13(e)]. More specifically, the Cu_7 configuration, which was discovered by Bickham *et al.* in 1999 through DFT calculations using the PBE functional, is actually the smallest structure that contains almost all the typical characteristics that a macroscopic structure (like the new structure we identified here) would have. Since these kinds of structural characteristics can lower the total energy of the system if relaxed using the PBE functional, for the same size of cells, the Cu_7 configuration has a lower energy than the Cu_4 configuration. To better understand the complex new structure, we also identify the primitive cell (12 atoms) of the new structure in one of the two orthogonal domains in the large defective supercell with 8000 atoms. More details are provided in the Supplemental Material [46]. This simplified structure, which has lower total energy per atom than the Cu_4 and Cu_7 configuration, turns out to be the most stable one of CuCl within the PBE functional.

After analyzing Cu clusters and structural relaxation results using the PBE-based potential, we, again, perform the same analysis using the deep-learning potential trained with the HSE data set. As depicted in Fig. 14(a), for the HSE-based potential, all the Cu clusters are rather small; even the top 10 largest ones only contain no more than four or five Cu atoms, which are significantly different from those zigzag chain structures in the representative configuration from MD simulations performed using the PBE-based potential [see Fig. 11(a)]. We also perform structural relaxations for the configuration at 0 K using the HSE-based potential [see Figs. 14(b) and 14(c)]. After relaxation, the structure from MD simulations returns to ideal zinc blende, which means that the off-center-like small Cu clusters are only formed by primarily instantaneous thermal fluctuations. We also evaluate the total energy of the new structure identified above compared to Cu_4, Cu_7, and zinc blende, using the HSE hybrid functional. We find that, in contrast to the PBE results, the simplified new structure becomes energetically unfavorable when using the HSE functional [46].

To distinguish the new defective structure from the ideal zinc-blende structure in a more quantitative way and to check if it is actually present in CuCl, we calculate the x-ray diffraction (XRD) patterns of these several structures of CuCl (see Fig. 15) with the VESTA program [47]. One can see that there is almost no difference in the XRD patterns between
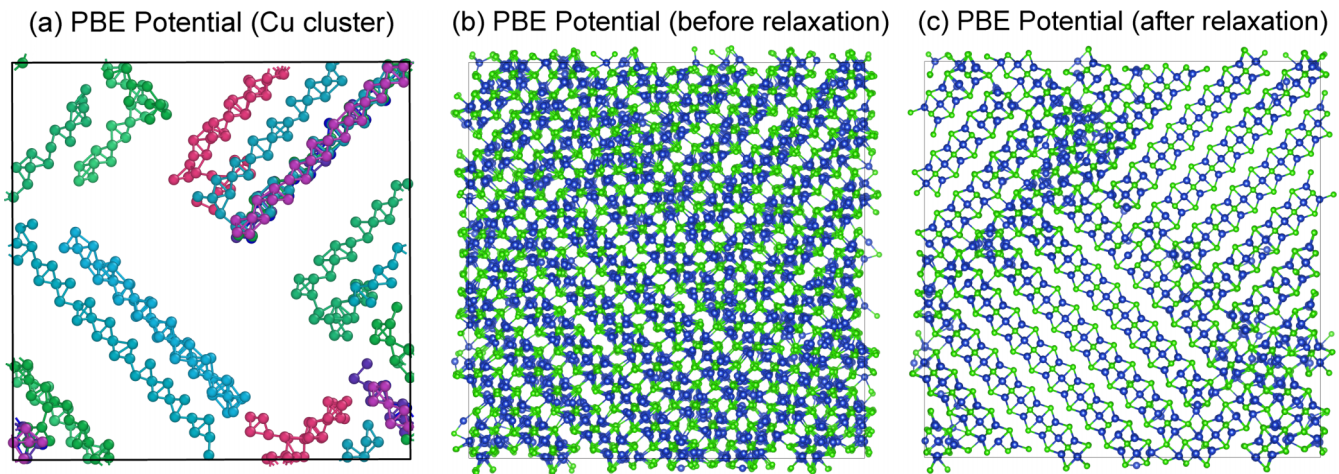
FIG. 11. (a) Cu cluster analysis of the equilibrium configurations from MD simulations performed at 300 K using the deep-learning potential trained with PBE data sets. All the Cl atoms are hidden and the Cu-Cu bond cutoff is set to 3.2 Å. For the sake of convenience, only the top ten largest Cu clusters are shown in each subgraph. Different colors are used to distinguish different clusters from each other. (b) Equilibrium configuration from MD simulations performed at 300 K using the deep-learning potential trained with PBE data sets. (c) Atomic structure of the configuration in (b) after structural relaxations (i.e., energy and force minimizations). The blue spheres depict Cu atoms and the green spheres represent Cl atoms.

the ideal zinc-blende structure and an equilibrium configuration from MD simulations performed at 300 K using the deep-learning potential trained with the HSE data set, as the off-center displacements in the HSE-based MD simulations are mostly caused by instantaneous thermal fluctuations. For the Cu_4 configuration, since the four displaced Cu atoms are localized in a relatively small region in the supercell, its XRD pattern is only slightly different from ideal zinc blende. While for the Cu_7 configuration and the new defective structure [PBE @ 300 K (relaxed)] we found, many other sharp characteristic peaks (e.g., the peaks within 10–

20°, slightly below, and above 28°) can be observed in their XRD patterns. However, by comparing with the experimentally measured XRD, it is apparent that the characteristic peaks of the defective configurations are completely absent. This unambiguously demonstrates that the defective cluster configurations as obtained from first-principles PBE calculations or the PBE-based deep-learning potential are unstable in reality; the exchange interactions are essential here, which can be properly treated by the HSE hybrid functional or the newly developed deep-learning potential of an HSE level of accuracy.
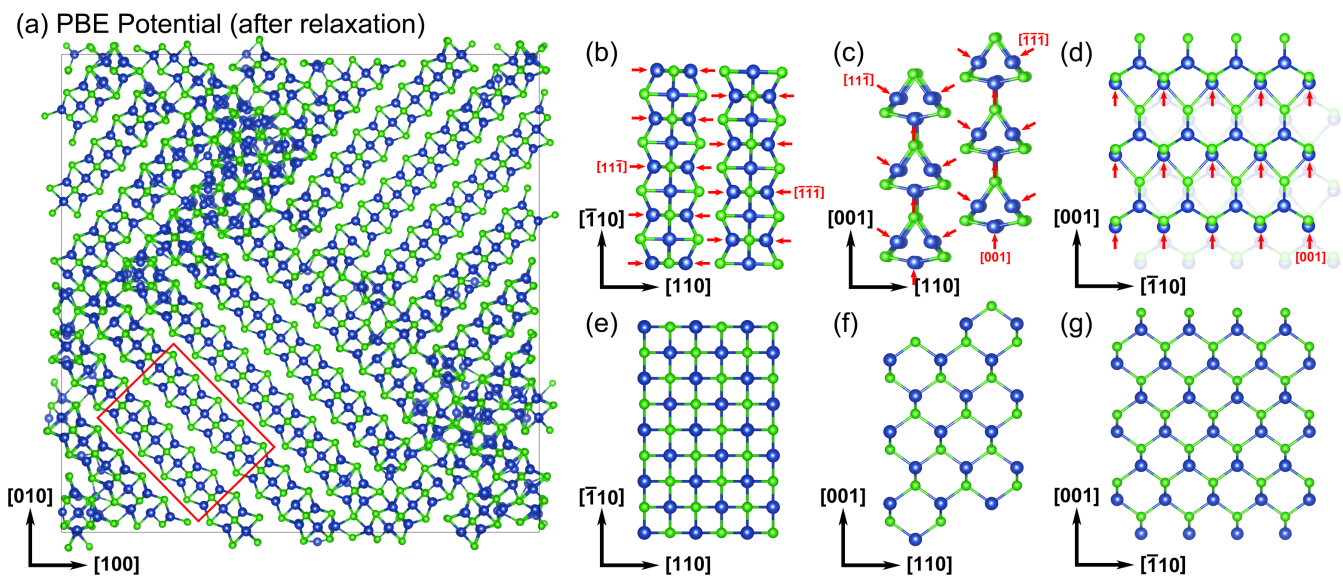

FIG. 12. (a) Atomic structure of a representative equilibrium configuration from MD simulations performed at 300 K using the deep-learning potential trained with the PBE data set. (b)–(d) Local structure extracted from the red box in (a), viewing from (b) [001] direction, (c) [$\bar{1}$10] direction, and (d) [110] direction. (e)–(g) Ideal zinc-blende structure for comparison, viewing from (e) [001] direction, (f) [$\bar{1}$10] direction, and (g) [110] direction. The red arrows and directions labeled depict the displacement directions of Cu atoms (blue spheres) in the local configuration of the new "defective" structure compared to the ideal zinc-blende structure.
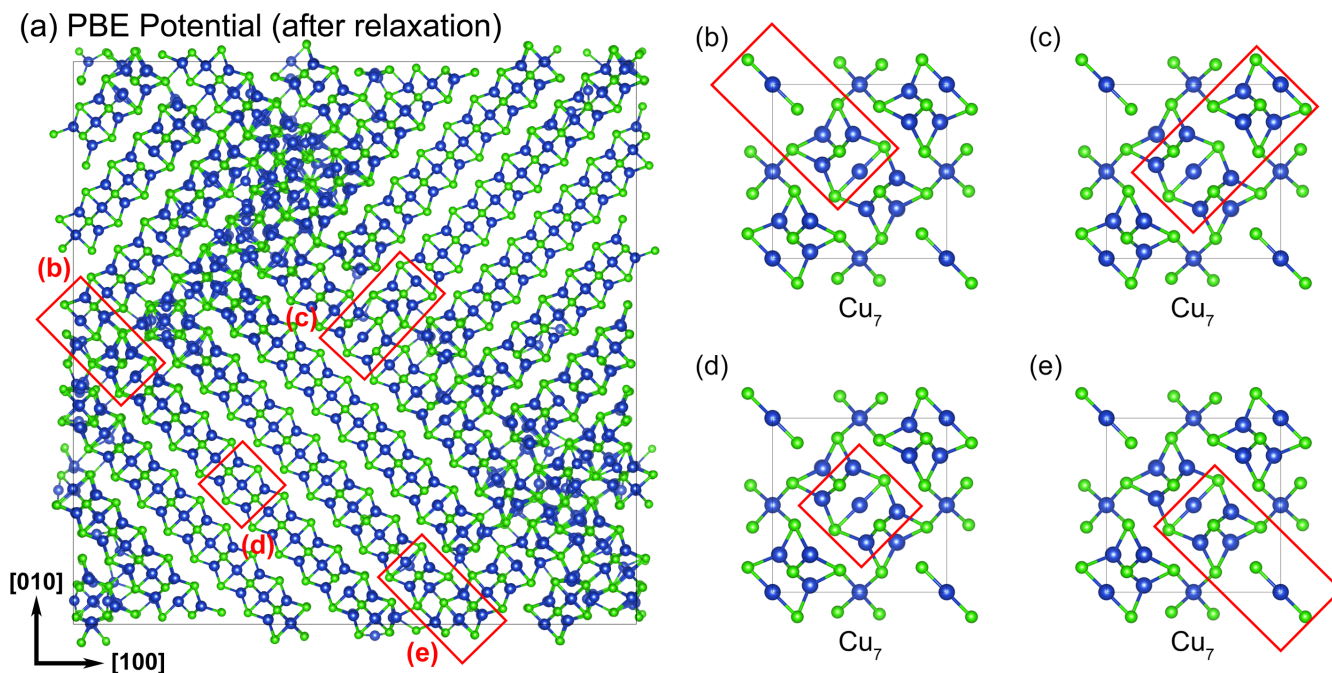
FIG. 13. (a) Atomic structure of a representative equilibrium configuration from MD simulations performed at 300 K using the deep-learning potential trained with the PBE data set. The red boxes with different labels mark several regions that are similar to those parts in the Cu_7 configuration (b)–(e).

IV. CONCLUSIONS

We have developed an accurate deep-learning potential for CuCl, which allows us to probe the off-center atomic displacements in CuCl at finite temperatures. This potential combines a high accuracy at the HSE level, which is essential for an accurate description of the structural and electronic properties of CuCl. With MD simulations using the newly developed potential, we found that around 10% of Cu are off center from the tetrahedral sites at room temperature, which is drastically lower than the result derived from a similar potential at the PBE level of accuracy.

With a careful cluster analysis, we found that there indeed exist large complex Cu cluster configurations (beyond Cu_4 and Cu_7) when exchange interactions are not taken into account (i.e., using the PBE-based potential). However,
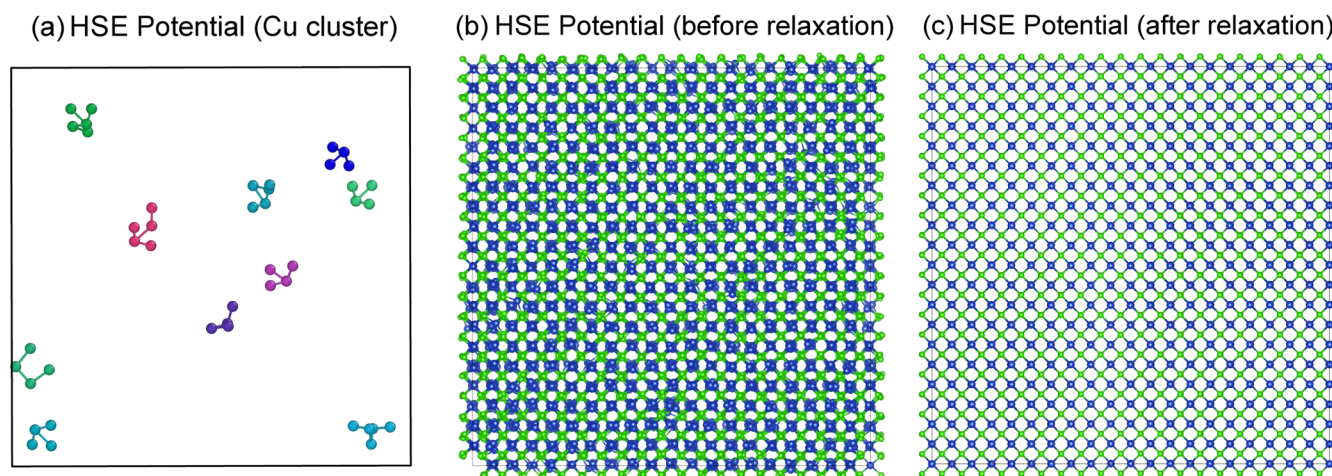

FIG. 14. (a) Cu cluster analysis of a representative equilibrium configuration from MD simulations performed at 300 K using the deep-learning potential trained with the HSE data set. All the Cl atoms are hidden and the Cu-Cu bond cutoff is set to 3.2 Å. For the sake of convenience, only the top 10 largest Cu clusters are shown in each subgraph. Different colors are used to distinguish different clusters from each other. (b) A representative equilibrium configuration from MD simulations performed at 300 K using the deep-learning potential trained with the HSE data set. (c) Atomic structure of the configuration in (b) after structural relaxations (i.e., energy and force minimizations). The blue spheres depict Cu atoms and the green spheres represent Cl atoms.
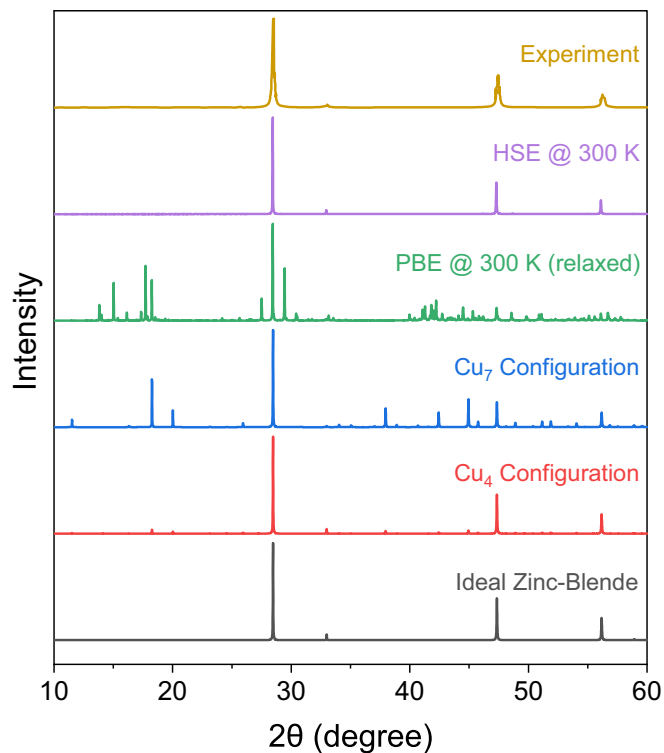
FIG. 15. X-ray diffraction (XRD) patterns of several kinds of structures of CuCl, calculated using the VESTA program [47]: equilibrium configurations from MD simulations performed at 300 K using the deep-learning potentials trained with HSE data sets (purple curve), PBE data sets (green curve, after relaxation), Cu_7 (blue curve), Cu_4 (red curve), and the ideal zinc-blende structure (black curve). The experimental XRD [48] of CuCl nanoparticles at temperature 25 °C (yellow curve) is depicted for comparison.

these clusters are unstable once exchange interactions are properly treated (i.e., using the HSE-based potential). Still, due to strong anharmonicity, thermal fluctuations could still lead to sizable off-center Cu displacements, leading to instantaneous small Cu clusters. Nevertheless, these cluster configurations are not stable or metastable in the ground state.

Therefore, we conclude that zinc-blende CuCl is indeed thermodynamically stable against off-center displacements of Cu atoms, despite the strong lattice anharmonicity. This conclusion should also apply to CuBr and CuI, since these two materials are less anharmonic. The important insights of strong lattice anharmonicity and its impact on the off-center displacements of Cu are expected to be relevant to various properties such as ferroelectricity [49,50] and superconductivity [51] in cuprous halides and other compounds, since the lattice anharmonicity may tune the critical temperature T_c of superconductors and the anharmonic damping can help to develop a microscopic description of softening of optical modes in the ferroelectric phase. Moreover, the newly developed highly accurate deep-learning potential enables atomistic simulations and computations of various properties of CuCl at finite temperatures, which constitutes an important basis for future atomistic modeling studies.

[1] J. Valenta, J. Dian, P. Gilliot, and B. Hönerlage, Photoluminescence and optical gain in CuBr semiconductor nanocrystals, Phys. Status Solidi B **224**, 313 (2001).

[2] D. Ahn and S. Lien Chuang, High optical gain of I–VII semiconductor quantum wells for efficient light-emitting devices, Appl. Phys. Lett. **102**, 121114 (2013).

[3] D. Ahn and S.-H. Park, Cuprous halides semiconductors as a new means for highly efficient light-emitting diodes, Sci. Rep. **6**, 20718 (2016).

[4] D. Azhikodan and T. Nautiyal, Enormous excitonic effects in bulk, mono- and bi- layers of cuprous halides using many-body perturbation technique, Solid State Commun. **265**, 41 (2017).

[5] M. Grundmann, F.-L. Schein, M. Lorenz, T. Böntgen, J. Lenzner, and H. von Wenckstern, Cuprous iodide: A p-type transparent semiconductor, history, and novel applications, Phys. Status Solidi A **210**, 1671 (2013).

[6] J. A. Christians, R. C. M. Fung, and P. V. Kamat, An inorganic hole conductor for organo-lead halide perovskite solar cells. Improved hole conductivity with copper iodide, J. Am. Chem. Soc. **136**, 758 (2014).

[7] G. A. Sepalage, S. Meyer, A. Pascoe, A. D. Scully, F. Huang, U. Bach, Y.-B. Cheng, and L. Spiccia, Copper(I) iodide as hole-conductor in planar perovskite solar cells: Probing the origin of J - V hysteresis, Adv. Funct. Mater. **25**, 5650 (2015).

[8] C. Yang, D. Souchay, M. Kneiß, M. Bogner, H. M. Wei, M. Lorenz, O. Oeckler, G. Benstetter, Y. Q. Fu, and M. Grundmann, Transparent flexible thermoelectric material based on non-toxic earth-abundant p-type copper iodide thin film, Nat. Commun. **8**, 16076 (2017).

[9] B. M. Morais Faustino, D. Gomes, J. Faria, T. Juntunen, G. Gaspar, C. Bianchi, A. Almeida, A. Marques, I. Tittonen, and I. Ferreira, CuI p-type thin films for highly transparent thermoelectric p-n modules, Sci. Rep. **8**, 6867 (2018).

[10] M. Almasoudi, A. Saeed, N. Salah, A. Alshahrie, P. M. Z. Hasan, A. Melaibari, and K. Koumoto, CuI: A promising halide for thermoelectric applications below 373 K, ACS Appl. Energy Mater. **5**, 10177 (2022).

[11] J. C. Phillips, *Bonds and Bands in Semiconductors*, 2nd ed. (Momentum Press, New York, 2009).

[12] S.-H. Wei, S.-B. Zhang, and A. Zunger, Off-Center Atomic Displacements in Zinc-Blende Semiconductor, Phys. Rev. Lett. **70**, 1639 (1993).

[13] C. H. Park and D. J. Chadi, Ground State Structural Anomalies in Cuprous Halides: CuCl, Phys. Rev. Lett. **76**, 2314 (1996).

[14] S. R. Bickham, J. D. Kress, L. A. Collins, and R. Stumpf, *Ab Initio* Molecular Dynamics Studies of Off-Center Displacements in CuCl, Phys. Rev. Lett. **83**, 568 (1999).

[15] A. Göbel, T. Ruf, M. Cardona, C. T. Lin, and J. C. Merle, Comment on "Ground State Structural Anomalies in Cuprous Halides: CuCl", Phys. Rev. Lett. **77**, 2591 (1996).

[16] M. Cardona, K. Syassen, and T. Ruf, Comment on "*Ab Initio* Molecular Dynamics Studies of Off-Center Displacements in CuCl", Phys. Rev. Lett. **84**, 4511 (2000).

[17] J. B. Boyce, T. M. Hayes, and J. C. Mikkelsen, Extended-x-ray-absorption-fine-structure investigation of mobile-ion density in superionic AgI, CuI, CuBr, and CuCl, Phys. Rev. B **23**, 2876 (1981).

[18] F. Altorfer, B. Graneli, P. Fischer, and W. Buhrer, An investigation of anharmonic atomic vibrations of γ-CuCl and γ-CuBr by powder neutron diffraction, J. Phys.: Condens. Matter **6**, 9949 (1994).

[19] C. Ulrich, A. Göbel, K. Syassen, and M. Cardona, Pressure-Induced Disappearance of the Raman Anomaly in CuCl, Phys. Rev. Lett. **82**, 351 (1999).

[20] Z.-H. Wang, S.-H. Wei, and X. Zhang, Comment on "wide-range-tunable p-type conductivity of transparent $CuI_{1-x}Br_x$ alloy", Adv. Funct. Mater. **32**, 2112765 (2022).

[21] Z.-H. Wang, X. Zhang, and S.-H. Wei, Origin of structural anomaly in cuprous halides, J. Phys. Chem. Lett. **13**, 11438 (2022).

[22] J. P. Perdew, K. Burke, and M. Ernzerhof, Generalized Gradient Approximation Made Simple, Phys. Rev. Lett. **77**, 3865 (1996).

[23] J. Heyd and G. E. Scuseria, Efficient hybrid density functional calculations in solids: Assessment of the Heyd–Scuseria–Ernzerhof screened Coulomb hybrid functional, J. Chem. Phys. **121**, 1187 (2004).

[24] J. Han, L. Zhang, R. Car, and W. E, Deep Potential: A general representation of a many-body potential energy surface, CiCP **23**, 629 (2018).

[25] L. Zhang, J. Han, H. Wang, R. Car, and W. E, Deep Potential Molecular Dynamics: A Scalable Model with the Accuracy of Quantum Mechanics, Phys. Rev. Lett. **120**, 143001 (2018).

[26] G. Kresse and J. Furthmüller, Efficient iterative schemes for *ab initio* total-energy calculations using a plane-wave basis set, Phys. Rev. B **54**, 11169 (1996).

[27] G. Kresse and D. Joubert, From ultrasoft pseudopotentials to the projector augmented-wave method, Phys. Rev. B **59**, 1758 (1999).

[28] X. Zhang, M. E. Turiansky, J.-X. Shen, and C. G. Van de Walle, Defect tolerance in halide perovskites: A first-principles perspective, J. Appl. Phys. **131**, 090901 (2022).

[29] H. Yu, X. Cai, Y. Yang, Z.-H. Wang, and S.-H. Wei, Band gap anomaly in cuprous halides, Comput. Mater. Sci. **203**, 111157 (2022).

[30] K. Saito, M. Hasuo, T. Hatano, and N. Nagasawa, Band gap energy and binding energies of Z3-excitions in CuCl, Solid State Commun. **94**, 33 (1995).

[31] H. Wang, L. Zhang, J. Han, and W. E, DeePMD-kit: A deep learning package for many-body potential energy representation and molecular dynamics, Comput. Phys. Commun. **228**, 178 (2018).

[32] Y. Zhang, H. Wang, W. Chen, J. Zeng, L. Zhang, H. Wang, and W. E, DP-GEN: A concurrent learning platform for the gener-ation of reliable deep learning based potential energy models, Comput. Phys. Commun. **253**, 107206 (2020).

[33] L. Zhang, J. Han, H. Wang, W. Saidi, R. Car, and W. E, End-to-end symmetry preserving inter-atomic potential energy model for finite and extended systems, in *Advances in Neural Information Processing Systems*, edited by S. Bengio, H. Wallach, H. Larochelle, K. Grauman, N. Cesa-Bianchi, and R. Garnett (Curran Associates, Inc., Red Hook, NY, 2018), Vol. 31.

[34] K. He, X. Zhang, S. Ren, and J. Sun, Deep residual learning for image recognition, *2016 IEEE Conference on Computer Vision and Pattern Recognition (CVPR)* (IEEE, Las Vegas, NV, 2016), pp. 770–778.

[35] D. P. Kingma and J. Ba, Adam: A method for stochastic optimization, arXiv:1412.6980.

[36] S. Hull and D. A. Keen, High-pressure polymorphism of the copper(I) halides: A neutron-diffraction study to ~10 GPa, Phys. Rev. B **50**, 5868 (1994).

[37] R. Hanson, J. Hallberg, and C. Schwab, Elastic and piezoelectric constants of the cuprous halides, Appl. Phys. Lett. **21**, 490 (1972).

[38] A. Togo and I. Tanaka, First principles phonon calculations in materials science, Scr. Mater. **108**, 1 (2015).

[39] Y.-C. Hu and H. Tanaka, Origin of the boson peak in amorphous solids, Nat. Phys. **18**, 669 (2022).

[40] M. Baggioli and A. Zaccone, Universal Origin of Boson Peak Vibrational Anomalies in Ordered Crystals and in Amorphous Materials, Phys. Rev. Lett. **122**, 145501 (2019).

[41] R. Milkus and A. Zaccone, Local inversion-symmetry breaking controls the boson peak in glasses and crystals, Phys. Rev. B **93**, 094204 (2016).

[42] S. Plimpton, Fast parallel algorithms for short-range molecular dynamics, J. Comput. Phys. **117**, 1 (1995).

[43] S. Nosé, A unified formulation of the constant temperature molecular dynamics methods, J. Chem. Phys. **81**, 511 (1984).

[44] W. G. Hoover, Canonical dynamics: Equilibrium phase-space distributions, Phys. Rev. A **31**, 1695 (1985).

[45] *CRC Handbook of Chemistry and Physics*, 97th ed., edited by W. M. Haynes, D. R. Lide, and T. J. Bruno (CRC Press, Boca Raton, FL, 2016).

[46] See Supplemental Material at http://link.aps.org/supplemental/10.1103/PhysRevMaterials.7.034601 for more details about the new structure.

[47] K. Momma and F. Izumi, *VESTA3* for three-dimensional visu-alization of crystal, volumetric and morphology data, J. Appl. Crystallogr. **44**, 1272 (2011).

[48] Y. Huang, F. Shen, J. La, G. Luo, J. Lai, C. Liu, and G. Chu, Synthesis and characterization of CuCl nanoparticles in deep eutectic solvents, Part. Sci. Technol. **31**, 81 (2013).

[49] T. Lanigan-Atkins, S. Yang, J. L. Niedziela, D. Bansal, A. F. May, A. A. Puretzky, J. Y. Y. Lin, D. M. Pajerowski, T. Hong, S. Chi, G. Ehlers, and O. Delaire, Extended anharmonic collapse of phonon dispersions in SnS and SnSe, Nat. Commun. **11**, 4430 (2020).

[50] L. Casella and A. Zaccone, Soft mode theory of ferroelectric phase transitions in the low-temperature phase, J. Phys.: Condens. Matter **33**, 165401 (2021).

[51] C. Setty, M. Baggioli, and A. Zaccone, Anharmonic phonon damping enhances the T_c of BCS-type superconductors, Phys. Rev. B **102**, 174506 (2020).

[52] https://bohrium.dp.tech